



# Crystalline palladium–cobalt alloy nanoassemblies with enhanced activity and stability for the formic acid oxidation reaction

Lu Zhang, Ling Wan, Yanrong Ma, Yu Chen\*, Yiming Zhou, Yawen Tang\*, Tianhong Lu

Jiangsu Key Laboratory of New Power Batteries, Laboratory of Electrochemistry, College of Chemistry and Materials Science, Nanjing Normal University, 1# Wenyuan Road, Nanjing 210046, PR China

## ARTICLE INFO

### Article history:

Received 28 November 2012  
Received in revised form 10 February 2013  
Accepted 25 February 2013  
Available online 4 March 2013

### Keywords:

3D network  
Palladium–cobalt alloy nanoassemblies  
Cyanogel  
Electrocatalytic activity  
Formic acid oxidation reaction

## ABSTRACT

In this work, we conveniently synthesize the three-dimensionally (3D) networks-like palladium–cobalt alloy nanoassemblies (Pd–Co ANAs) through a simple simultaneous reduction reaction with sodium borohydride using inorganic  $K_2PdCl_4/K_3Co(CN)_6$  cyanogel as reaction precursors, and clarify the formation mechanism of 3D networks structure and generation mechanism of Pd–Co alloy at room temperature. The morphology, structure, size and composition of the Pd–Co ANAs are characterized by scanning electron microscopy (SEM), transmission electron microscopy (TEM), selected area electron diffraction (SAED), energy dispersive spectrum (EDS), X-ray diffraction (XRD) and X-ray photoelectron spectroscopy (XPS). Cyclic voltammetry, chronoamperometry and CO-stripping voltammetry tests demonstrate the Pd–Co ANAs have higher electrocatalytic activity, better electrochemical stability, and higher resistance to CO poisoning over single-component Pd nanoparticles for the formic acid oxidation reaction (FAOR) owing to their unique 3D structure and alloy property.

© 2013 Elsevier B.V. All rights reserved.

## 1. Introduction

Fuel cells operated with small organic molecule as the anode fuel source have gained significant interest as a viable alternative to hydrogen fuel cells for the portable power applications [1–7]. With low fuel crossover and high energy density, direct formic acid fuel cells (DFAFCs) are expected to be among the first commercial applications of various fuel cells [8–12]. Pd-catalyzed formic acid oxidation reaction (FAOR) is one of the most important reactions in DFAFCs. However, CO poisoning and aggregation/growth of Pd nanoparticles during the anode reaction rapidly degrade the performance of DFAFCs [13]. At present, one effective strategy for improving the catalyst's performance (catalytic activity and CO tolerance) is to incorporate an early transition metal element (M = cobalt, nickel, iron and ruthenium) into the Pd structure to make Pd–M alloys, which can be ascribed to the modification of the Pd electronic structure as well as the correlation of the ligand and strain effects [14–17].

Until now, the synthesis of the Pd–M nanoparticles with a high alloying degree is one of the most challenging tasks because of their distinct standard reduction potential and atom size between different metals [17–19]. For example, the conventionally wet-chemical

synthetic process usually results in the exterior M-enrichment of Pd–M nanoparticles due to the preferential reduction of Pd<sup>II</sup> precursor [20]. The exterior M-enriched structure decreases the electrocatalytic activity of Pd–M nanoparticles due to the decrease in Pd active sites. To produce Pd–M alloy nanoparticles with desirable composition, the high-temperature thermal treatment is typically used to increase the alloying degree [21–23]. However, such thermal treatment unavoidably causes particle aggregation or sintering, thus decreasing the mass activity of Pd–M nanoparticles.

On the other hand, the durability of electrocatalysts has been recognized as one of the most important issues to be addressed before the commercialization of fuel cells [24–27]. Recent investigations have indicated that three-dimensional (3D) noble metal nanoassemblies can effectively improve the durability of electrocatalysts because of their excellent electrochemical self-stability [28–30]. Essentially, no individual nanoparticle exists in 3D nanoassemblies due to the particular interconnected structure, which effectively restrains Ostwald ripening effect. Meanwhile, the abundant defect atoms in nanoassemblies, including steps, edges and kinks, usually are much more active than terrace atoms, and thus contribute to the significantly enhanced electrocatalytic activity. Till now, large numbers of 3D noble metal nanoassemblies have been synthesized by dealloying [31] and templating [32,33] methods. However, the reactant is expensive and harm to environment, or the approach is complication and low yields so that it cannot be scaled up readily.

\* Corresponding authors. Tel.: +86 25 85891651; fax: +86 25 83243286.

E-mail addresses: [ndchenyu@yahoo.cn](mailto:ndchenyu@yahoo.cn) (Y. Chen), [tangyawen@njnu.edu.cn](mailto:tangyawen@njnu.edu.cn) (Y. Tang).

Cyanogels, a coordination polymer made from a mixture of a tetrachlorometalates ( $[RCl_4]^{2-}$ ,  $R = Pd, Pt$ ) and a transition metal cyanometalate ( $[M(CN)_n]^{2-/3-}$ , ( $n = 4, 6$ ;  $M = Co, Fe, Ru, Os, Ni, Cr$ )) in aqueous solution, are a special class of 3D double-metal cyanide [28,34–38]. By means of their particular properties such as the 3D characteristic backbone, solid nature, and uniform distribution of the two kinds of metal ions on the cyanogel backbone, the 3D noble metal nanoassemblies may be obtained easily using cyanogel as reaction precursor [39]. Herein, we report the simple room-temperature synthesis of the networks-like palladium–cobalt nanoassemblies (Pd–Co ANAs) with high alloying degree using the  $K_2PdCl_4/K_3Co(CN)_6$  cyanogel as reaction precursor via simple  $NaBH_4$  reduction method. The synthesized crystalline Pd–Co ANAs exhibit enhanced stability and electrocatalytic activity for the FAOR due to their particular 3D network structure and high alloying degree.

## 2. Experimental

### 2.1. Synthesis of palladium–cobalt alloy nanoassemblies

2 mL of 50 mM  $K_2PdCl_4$  and 1 mL of 50 mM  $K_3Co(CN)_6$  aqueous solutions were mixed at room temperature. After 2 h, the light yellow  $K_2PdCl_4/K_3Co(CN)_6$  cyanogel was formed. Then, 3 mL  $0.2\text{ g mL}^{-1}$   $NaBH_4$  solution was added into  $K_2PdCl_4/K_3Co(CN)_6$  cyanogel. After reaction, the black palladium–cobalt alloy nanoassemblies (Pd–Co ANAs) were separated by centrifugation, washed consecutively with water, 0.1 M  $HClO_4$  solution and water, and then dried at  $40^\circ\text{C}$  in a vacuum oven for 12 h. The acid wash process could ensure the removal of unalloyed Co. For comparison, the single-component Pd nanoparticles (termed as Pd-control) were prepared using  $K_2PdCl_4$  as reaction precursor under similar experimental conditions. The Pd–Co nanoparticles (termed as Pd–Co-control) were also prepared using the mixture of  $K_2PdCl_4$  and  $CoCl_2$  as reaction precursors under similar experimental conditions.

### 2.2. Physical characterization

Scanning electron microscopy (SEM) images were captured on a Hitachi S-4800 scanning electron microscope, operating at 5 kV. The morphology and particle size of catalysts were investigated using a JEOL JEM-2010 transmission electron microscope (TEM) operated at 200 kV accelerating potential. X-ray photoelectron spectroscopy (XPS) measurements were carried out on a Thermo VG Scientific ESCALAB 250 spectrometer with a monochromatic Al K $\alpha$  X-ray source (1486.6 eV photons). The binding energy was calibrated with respect to C1s at 284.8 eV. The X-ray diffraction (XRD) patterns were obtained with a Model D/max-rC X-ray diffractometer using Cu K $\alpha$  radiation source ( $\lambda = 1.5406\text{ \AA}$ ) and operating at 40 kV and 100 mA. The composition of the catalysts was determined using the energy dispersive spectrum (EDS) technique. The UV–vis spectra were recorded at room temperature on a UV3600 spectrophotometer equipped with 1.0 cm quartz cells. Fourier transform infrared (FT-IR) spectra were recorded with a Nicolet 520 SXTIR spectrometer.

### 2.3. Electrochemical measurement

All electrochemical experiments were carried out on a CHI 660 C electrochemical workstation (CH Instruments, Shanghai, Chenghua Co.). A standard three-electrode system was used for all electrochemical experiments, which consisted of a platinum wire as the auxiliary electrode, a saturated calomel reference electrode (SCE) protected by Luggin capillary with KCl solution as the reference electrode, and a catalyst modified glassy carbon electrode as the

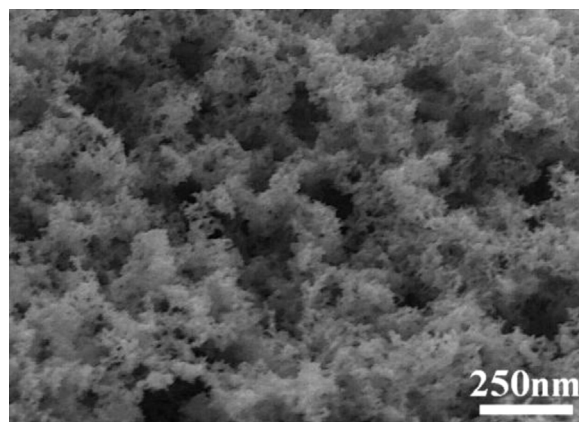


Fig. 1. SEM image of the Pd–Co ANAs.

working electrode. Potentials in this study were reported with respect to SCE. For preparation of working electrode, typical process follows the previous procedure reported [40]. An evenly distributed suspension of catalyst was prepared by ultrasonic mixing the 4 mg catalyst and 2 mL  $H_2O$  for 30 min, and 6  $\mu\text{L}$  of the resultant suspension was laid on the surface of the glassy carbon electrode (3 mm diameter,  $0.07\text{ cm}^2$ ). After drying at  $40^\circ\text{C}$ , 2  $\mu\text{L}$  of Nafion (5 wt.%) solution was covered on the surface of electrode and allowed to dry again. Thus, the working electrode was obtained, and the specific loading of metal on the electrode was about  $12\text{ }\mu\text{g}$ . Electrochemical measurements were performed in 0.5 M  $N_2$ -saturated  $H_2SO_4$  solution with or without 0.5 M  $HCOOH$ . CO-stripping voltammetry tests were performed according to previous procedure reported [17,41]. All the electrochemical measurements were carried out at  $30 \pm 1^\circ\text{C}$ .

## 3. Results and discussion

### 3.1. Synthesis and characterization of palladium–cobalt alloy nanoassemblies

In a typical synthesis, 2 mL of 50 mM  $K_2PdCl_4$  and 1 mL of 50 mM  $K_3Co(CN)_6$  aqueous solutions were mixed at room temperature, which generated the light yellow  $K_2PdCl_4/K_3Co(CN)_6$  cyanogel with 3D characteristic backbone (Supplementary data, Fig. S1). Typically, the positions of the  $Pd(II) \rightarrow Co(III)$  intervalent charge transfer transition peak (328 nm, Supplementary data, Fig. S2) and stretching vibration peak of bridging cyano group ( $2200\text{ cm}^{-1}$ , Supplementary data, Fig. S3) were consistent with the previous report [42]. After the addition of  $NaBH_4$  solution, the Pd–Co ANAs were conveniently obtained (details see Section 2). As shown by SEM image in Fig. 1, the porous Pd–Co ANAs have a coral-like morphology. It is clear that  $Pd^{II}$  and  $Co^{III}$  species concentrate on the 3D backbone of cyanogel rather than disperse uniformly in water. Upon reduction, a larger number of metal nuclei are developed at the 3D backbone of  $K_2PdCl_4/K_3Co(CN)_6$  cyanogel. Due to the minimal distance between individual metal nuclei, the individual metal nucleus preferentially connects each other one-by-one along backbone direction of cyanogel, which results in the formation of interconnected Pd–Co nanoassemblies with 3D networks structure.

The structural features of the Pd–Co ANAs were further investigated by TEM. As observed, small primary nanoparticles are interconnected to each other to form 3D nanoassemblies with abundant pores (Fig. 2A). Selected area electron diffraction (SAED) image shows an irregularly and discretely dotted pattern (insert in Fig. 2A), indicating the polycrystalline Pd–Co ANAs are composed of single crystal nanoparticles. Further high-resolution TEM (HRTEM) image shows the obvious lattice fringes and large numbers of the

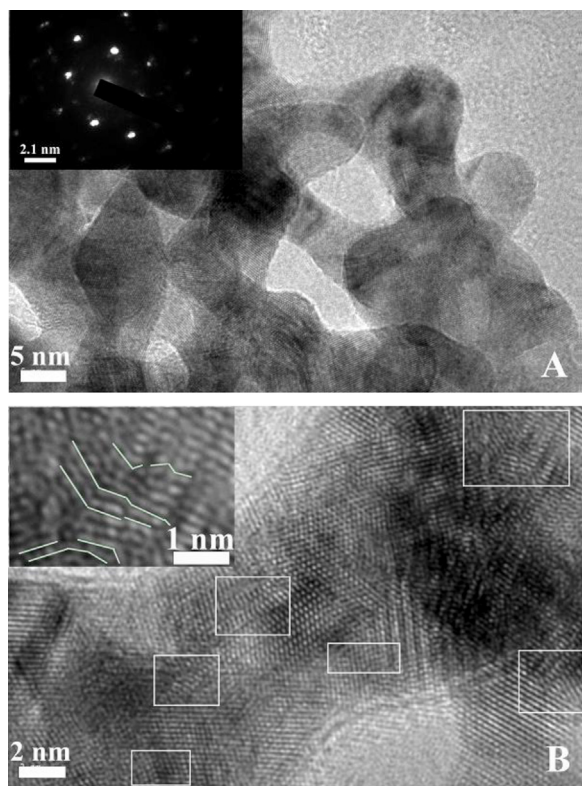


**Fig. 2.** (A) TEM image of the Pd–Co ANAs. Insert shows SAED image. (B) HRTEM image of the Pd–Co ANAs. Insert shows the enlarge image of the squared area selected randomly.

defects such as boundary, vacancy and dislocation (Fig. 2B and insert). The high density of defects may effectively improve catalyst's catalytic activity due to the open coordination nature of defect atom [43–45].

The composition and structure of the Pd–Co ANAs were investigated firstly by EDS and XRD. The EDS measurement shows Pd/Co atomic ratio in the Pd–Co ANAs is 86.3:13.7 (Fig. 3A), lower than that in the  $K_2PdCl_4/K_3Co(CN)_6$  cyanogel (2:1), demonstrating acid wash process can effectively remove unalloyed Co. XRD pattern of the Pd–Co ANAs shows a typical face-centered-cubic (fcc) pattern (Fig. 3B). Compared to the single-component Pd nanoparticles (i.e., Pd-control) obtained by the controlled experiment, all diffraction peaks in the Pd–Co ANAs shift to higher angle, indicating a lattice contraction due to the alloying of Pd with Co. For Pd–Co nanoparticles (i.e., Pd–Co-control) obtained by the controlled experiment, however, no obvious diffraction peak shift is observed compared to the single-component Pd nanoparticles, indicating no Pd–Co alloy is achieved. This indicates that the self-properties of  $K_2PdCl_4/K_3Co(CN)_6$  cyanogel play very important roles in the formation of Pd–Co alloy. It is clear that  $Pd^{II}$  and  $Co^{III}$  species uniformly mix at the atom-scale and concentrate on the cyanogel backbone. The intimate interaction of precursor  $Pd^{II}$  and  $Co^{III}$  species may induce a good mixture of Pd and Co crystal nuclei after  $NaBH_4$  reduction. Meanwhile, the solid nature of cyanogel can effectively restrain the Brownian motion of generated Pd and Co crystal nuclei, resulting in good combination between Pd and Co nuclei. The two factors benefit the formation of Pd–Co alloy even under room temperature conditions. The lattice parameter of the single-component Pd fcc phase is 0.3914 nm, while that of the Pd–Co ANWs is 0.3868 nm. Using Vegard's law [46,47], the alloying Co content in the Pd–Co ANAs (with respect to Pd) is calculated to be 12.3 at.%, in consistent with the EDS composition (atomic ratio of Co and Pd is 13.5:86.5). According to Scherrer equation, the average particle sizes,  $d_{XRD}$ , of the Pd–Co ANAs and Pd-control are calculated to be 3.9 and 6.9 nm, respectively. Furthermore, the surface

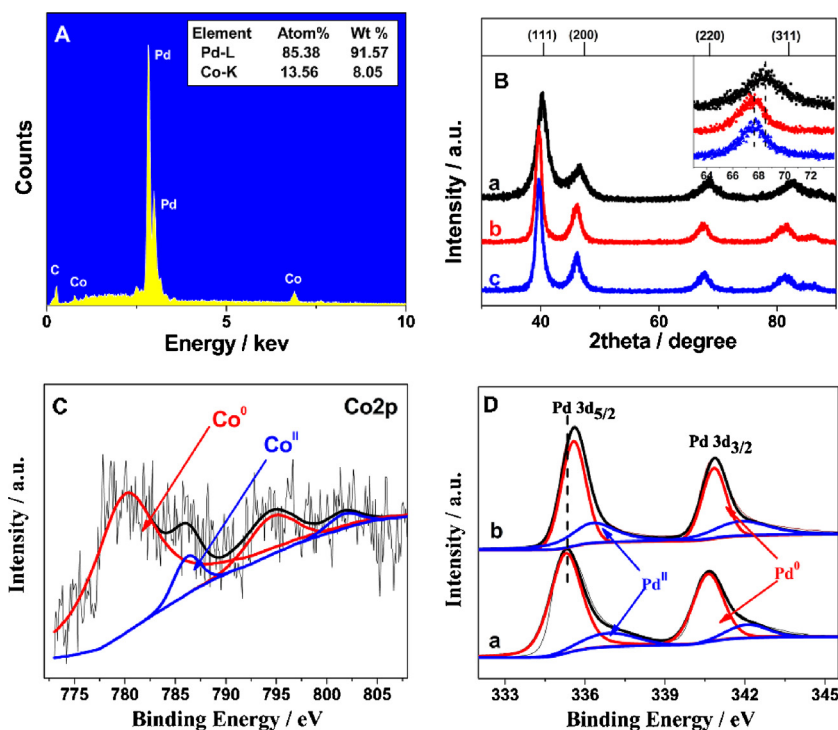


**Fig. 3.** (A) EDS spectrum of the Pd–Co ANAs. (B) XRD patterns of (a) the Pd–Co ANAs, (b) Pd-control and (c) Pd–Co-control. (C) XPS spectrum of the Pd–Co ANAs in the Co2p region. (D) XPS spectrum of (a) the Pd–Co ANAs and (b) Pd-control in the Pd3d region.



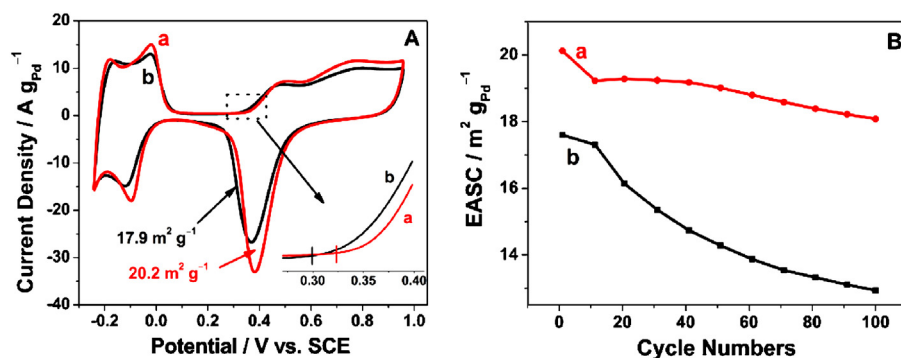


**Fig. 4.** (A) Cyclic voltammograms of (a) the Pd-Co ANAs and (b) Pd-control in N<sub>2</sub>-saturated 0.1 M HClO<sub>4</sub> solution at the scan rate of 50 mV s<sup>-1</sup>. (B) The ECASA vs. cycle numbers of (a) the Pd-Co ANAs and (b) Pd-control.

composition and electronic structure of the Pd-Co ANAs were investigated by XPS. Co/Pd atom ratio at the Pd-Co ANAs surface is measured to be 13.1:86.9 (Fig. S4), in consistent with the atomic fraction of alloying Co in the Pd-Co ANAs calculated from XRD. Meanwhile, the predominant Co<sup>0</sup> 2p<sub>1/2</sub> and Co<sup>0</sup> 2p<sub>3/2</sub> peaks are clearly observed in the Co 2p region (Fig. 3C), further confirming the formation of Pd-Co alloy. The Pd 3d binding energy in the Pd-Co ANAs negatively shift ca. 0.29 eV compared to that in Pd-control (Fig. 3D). The shift of the Pd 3d binding energy in the Pd-Co ANAs indicates the evident change in the Pd electronic structure, which is ascribed to the charge transfer between Co and Pd. By measuring the relative peak areas, the percentage of Pd<sup>0</sup> species in the Pd-Co ANAs is calculated to be 83.1%, much higher than that in the Pd-control (66.5%), indicating that the Pd-Co ANAs have a weaker oxophilicity than the Pd-control due to the downshift of d-band center of the Pd-Co ANAs [28,48–50], in agreement with the prediction of d-band center theory (i.e., lowering of the d-band center results in the decrease in interaction strength of the various adsorbates to the substrate) [51,52].

### 3.2. Electrochemical tests

Fig. 4A shows cyclic voltammograms of the Pd-Co ANAs and Pd-control in N<sub>2</sub>-saturated 0.1 M HClO<sub>4</sub> solution at 50 mV s<sup>-1</sup>. Onset oxidation potential of the Pd-Co ANAs shifts positively ca. 25 mV compared to the Pd-control, suggesting the alloying of Pd with Co content inhibits the chemisorption of hydroxyl species [53,54]. Since adsorbed hydroxyl species inhibit the FAOR, the lower hydroxyl surface coverage at the Pd-Co ANAs, offering more free active sites for the FAOR, may lead to an enhancement in the FAOR kinetics. The electrochemically active surface areas (ECASA) of the Pd-Co ANAs and Pd-control are calculated to be 20.2 and 17.9 m<sup>2</sup> g<sub>Pd</sub><sup>-1</sup> by integrating the coulometry of “Pd<sup>II</sup> reduction” in 0.3–0.5 V, respectively [55]. The electrochemical stabilities of the Pd-Co ANAs and Pd-control were evaluated by applying continuous potential scans. After 100 CV cycles, the ECASA of the Pd-Co ANAs lost approximately 10.2% of the initial value, much smaller than that in Pd-control (26.8%) (Fig. 4B), demonstrating that the Pd-Co ANAs show a greater stability for the electrochemical

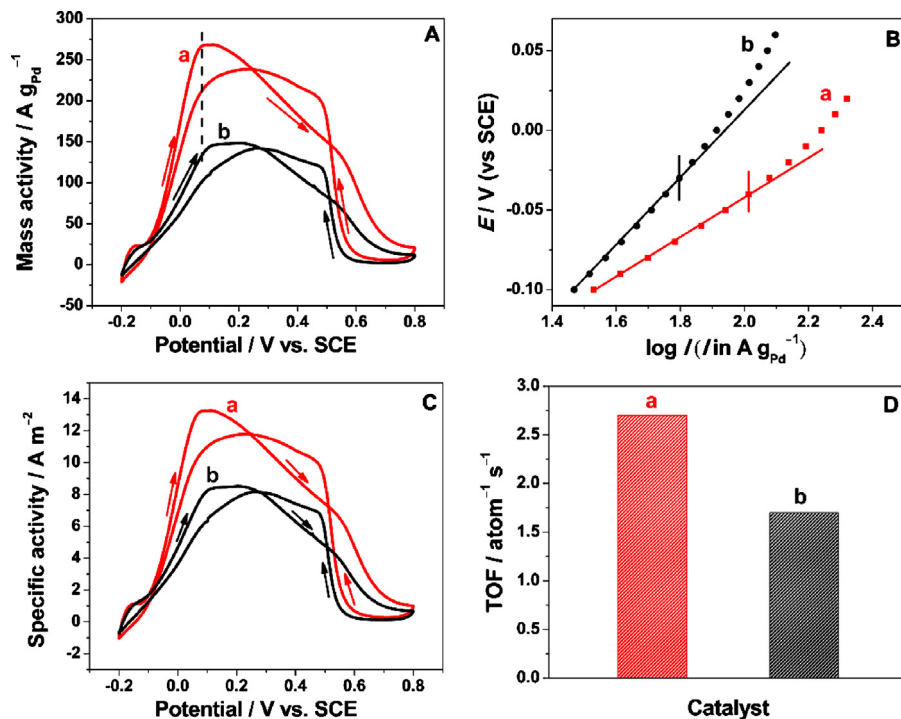
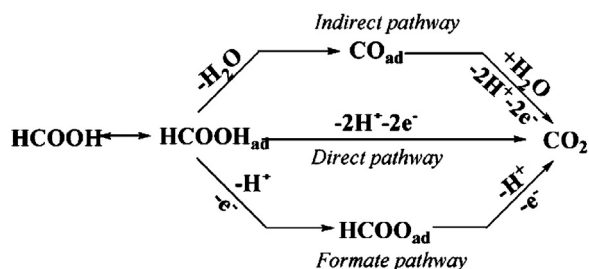


**Fig. 5.** (A) Mass activity of (a) the Pd-Co ANAs, (b) Pd-control in 0.5 M HCOOH + 0.5 M H<sub>2</sub>SO<sub>4</sub> solution at the scan rate of 50 mV s<sup>-1</sup>. (B) Tafel plots of log I vs. E for the FAOR at (a) the Pd-Co ANAs and (b) Pd-control in electrochemical control area. (C) Specific activity of (a) the Pd-Co ANAs and (b) Pd-control in 0.5 M HCOOH + 0.5 M H<sub>2</sub>SO<sub>4</sub> solution at the scan rate of 50 mV s<sup>-1</sup>. (D) The TOF of (a) the Pd-Co ANAs and (b) Pd-control at 0.1 V.



**Scheme 1.** Schematic description of the “triple-path way” reaction mechanism for the FAOR.

application than Pd-control. Due to the interconnected 3D structure, no individual Pd particle exists in the Pd-Co ANAs, which effectively restrains Ostwald ripening effect and consequently improves the self-stability of the Pd-Co ANAs [28,39,49,56].

Fig. 5A depicts the mass activities of the Pd-Co ANAs and Pd-control for the FAOR. In the positive scan direction, the peak potential of the FAOR at the Pd-Co ANAs negatively shifts ca. 40 mV compared to that at the Pd-control. The corresponding anodic peak current at the Pd-Co ANAs ( $267.0 \text{ A g}_{\text{Pd}}^{-1}$ ) is almost 1.8 times higher than that of Pd-control ( $148.5 \text{ A g}_{\text{Pd}}^{-1}$ ). In general, the mass activity can be taken as an index to assess the applicability (i.e., metal utilization) of the catalyst for the FAOR [57,58]. Thus, the lower oxidation peak potential and higher oxidation peak current show that the Pd-Co ANAs have higher electrocatalytic performance than the Pd-control, which may lead to the earlier commercialization of DFAFCs. Indeed, the Pd-Co ANAs have also much better performance than the commercial Pd black in terms of mass activity (Supplementary data, Fig. S5), further confirming the Pd-Co ANAs hold promise as potentially practical anodic electrocatalyst for DFAFCs.

Fig. 5B shows the Tafel plots of  $\log I$  vs.  $E$  for the FAOR at the Pd-Co ANAs and Pd-control in electrochemical control region. In lower output current region, both curves keep consistent with Tafel linear relationship. Under the same output voltage, the Pd-Co ANAs show a higher output current with respect to the Pd-control, namely, the slope of  $\log I$  vs.  $E$  curve at the Pd-Co ANAs is smaller at the Pd-Co ANAs. Moreover, the polarization over-potential at the Pd-control occurs at lower output current density. These results exhibit that the FAOR at the Pd-Co ANAs has a faster kinetic rate. FAOR obeys a triple-path mechanism in an acidic electrolyte (Scheme 1) [41,48,59,60]: (i) A direct pathway, in which formic acid is oxidized directly into  $\text{CO}_2$ ; (ii) A indirect pathway, via  $\text{CO}_{\text{ads}}$  formation and oxidation; (iii) A formate pathway, involving the formation and subsequent oxidation of formate to  $\text{CO}_2$ . The previous studies have demonstrated that the lower of 3d electron density of

Pd atom results in a decrease in adsorption energy of the formate intermediate, which enhances the rate of the FAOR via the direct path [57]. Thus, the change of Pd electronic structure in the Pd-Co ANAs improves the FAOR kinetics.

It is well known that the specific activity of catalyst can effectively evaluate the actual value of the intrinsic activity. As shown in Fig. 5C, specific peak current density of the Pd-Co ANAs ( $13.2 \text{ A m}^{-2}$ ) also exhibits nearly 1.6 times larger than that of the Pd-control ( $8.3 \text{ A m}^{-2}$ ). We further analyzed the turnover frequency (TOF) of the Pd-Co ANAs and Pd-control for the FAOR at 0.1 V according to Eq. (1) [61–64]. The TOF value gives the number of formic acid molecules formed per second per Pd surface site, assuming that all surface Pd atoms are active.

$$\text{TOF} = \frac{i_k}{neN_s} \quad (1)$$

where  $i_k$  is the specific current density,  $n$  is the number of electrons transferred,  $e$  is elementary charge, and  $N_s$  is atomic surface density. As shown in Fig. 5D, the Pd-Co ANAs show an enhancement in TOF than the reference Pd-control by a factor of 1.6 ( $2.7 \text{ atom}^{-1} \text{ s}^{-1}$  vs.  $1.7 \text{ atom}^{-1} \text{ s}^{-1}$ ) at 0.1 V potential. The improved activity of the Pd-Co ANAs for the FAOR may be ascribed to the following reasons: (i) the lower chemisorption of hydroxyl species, which offers more free active sites for the FAOR; (ii) the change in Pd electronic structure, which facilitates the direct path of formic acid oxidation; (iii) the abundant defects, which provides much more active sites for the FAOR.

To evaluate the electrocatalytic stabilities of catalysts, the chronoamperometry tests were conducted. Fig. 6A shows the chronoamperometric curves of 0.5 M  $\text{HCOOH} + 0.5 \text{ M H}_2\text{SO}_4$  solution at the Pd-Co ANAs and Pd-control at 0.1 V potential. After 3000 s, the oxidation currents of the FAOR at the Pd-Co ANAs and Pd-control decrease to 33.2% and 17.2% of their initial value (taken at 20 s to avoid the contribution of the double-layer discharge and hydrogen adsorption) [41,65], respectively. This fact indicates the durability of the Pd-Co ANAs is much better than that of the Pd-control. After the chronoamperometry run, XPS measurements show that the metallic Pd is still the predominant species in both the Pd-Co ANAs and Pd-control catalysts (Supplementary data, Fig. S6). Meanwhile, the Co/Pd atom ratio in the Pd-Co ANAs is measured to be 10.2:89.8 (Supplementary data, Fig. S7) after the chronoamperometry run, which is close to that the initial Pd-Co ANAs (13.1:86.9). Thus, the degradation of catalytic performance cannot mainly be ascribed to the dissolution of metallic Pd under present experiment conditions. In general, the degradation of catalytic performance originates from Pd nanoparticles migration/agglomeration and CO poisoning during the anode reaction. After the chronoamperometry run, the Pd-Co ANAs and Pd-control

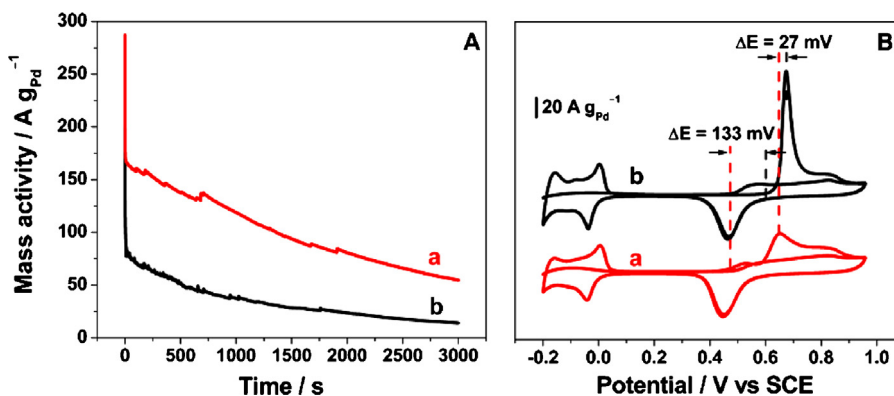


**Fig. 6.** (A) Chronoamperometry curves of (a) the Pd-Co ANAs and (b) Pd-control in 0.5 M  $\text{HCOOH} + 0.5 \text{ M H}_2\text{SO}_4$  solution at 0.1 V. (B) Cyclic voltammograms of pre-adsorbed CO at (a) the Pd-Co ANAs and (b) Pd-control in 0.5 M  $\text{H}_2\text{SO}_4$  solution at the scan rate of  $50 \text{ mV s}^{-1}$ .

catalysts retain 93.8% and 76.1% of the initial ECASA, respectively (Supplementary data, Fig. S8). The fact confirms that the interconnected 3D structure of the Pd–Co ANAs can effectively restrain Ostwald ripening effect, leading to a remarkably high stability of the Pd–Co ANAs in comparison with the Pd-control. Since CO poisoning is also one of the factors restraining the FAOR activity, we compared the CO<sub>ad</sub> oxidation behaviors at the Pd–Co ANAs and Pd-control catalysts. As shown in Fig. 6B, the peak current of CO oxidation at the Pd–Co ANAs is about 3 times lower than that at Pd-control. Moreover, the onset potential and peak potential of CO oxidation at the Pd–Co ANAs negatively shift ca. 133 and 27 mV compared to that at the Pd-control, indicating that the Pd–Co ANAs have the priority for CO oxidation [66]. The present CO-stripping tests indicate the change in Pd electronic structure at the Pd–Co ANAs results in a dramatic diminution in the affinity of CO, in consistent with the prediction of d-band center theory [51,52]. Moreover, the existence of Co also likely facilitates the effective CO removal according to bifunctional mechanism [16]. Thus, the good electrochemical self-stability and high CO tolerance of the Pd–Co ANAs are responsible for excellent durability of the Pd–Co ANAs for the FAOR.

#### 4. Conclusion

In summary, we have successfully synthesized Pd–Co ANAs through a facile cyanogel-reduction method. This simple, mild, template-free, organic molecules-free cyanogel-reduction route is an attractive choice for the facile large-scale production of the networks-like Pd–M alloy nanoassemblies. Due to the unique 3D networks structure, the abundant defects in nanoassemblies and the change of the Pd electronic structure, the Pd–Co ANAs exhibit better electrochemical stability, superior CO tolerant ability and higher electrocatalytic activity over single-component Pd nanoparticles for the FAOR. In the future, these particular 3D Pd–M alloy nanoassemblies potentially hold promise in various fields such as fuel cells and heterogeneous catalysis.

#### Acknowledgments

The authors are grateful for the financial support of NSFC (21073094 and 21273116), the United Fund of NSFC and Yunnan Province (U1137602), Industry-Academia Cooperation Innovation Fund Project of Jiangsu Province (BY2012001), and a project funded by the Priority Academic Program Development of Jiangsu Higher Education Institutions.

#### Appendix A. Supplementary data

Supplementary data associated with this article can be found, in the online version, at <http://dx.doi.org/10.1016/j.apcatb.2013.02.051>.

#### References

- [1] X. Yang, Q. Yang, J. Xu, C.S. Lee, *Journal of Materials Chemistry* 22 (2012) 8057–8062.
- [2] H. Li, G. Chang, Y. Zhang, J. Tian, S. Liu, Y. Luo, A.M. Asiri, A.O. Al-Youbi, X. Sun, *Catalysis Science & Technology* 2 (2012) 1153–1156.
- [3] D. Tu, B. Wu, B. Wang, C. Deng, Y. Gao, *Applied Catalysis B: Environmental* 103 (2011) 163–168.
- [4] M. Ren, Y. Kang, W. He, Z. Zou, X. Xue, D.L. Akins, H. Yang, S. Feng, *Applied Catalysis B: Environmental* 104 (2011) 49–53.
- [5] E. Antolini, J.R.C. Salgado, E.R. Gonzalez, *Applied Catalysis B: Environmental* 63 (2006) 137–149.
- [6] F. Colmati, E. Antolini, E.R. Gonzalez, *Applied Catalysis B: Environmental* 73 (2007) 106–115.
- [7] A. Serov, C. Kwak, *Applied Catalysis B: Environmental* 91 (2009) 1–10.
- [8] C.H. Chen, W.J. Liou, H.M. Lin, S.H. Wu, A. Borodzinski, L. Stobinski, P. Kedzierzawski, *Fuel Cells* 10 (2010) 227–233.
- [9] X. Yu, P.G. Pickup, *Journal of Power Sources* 182 (2008) 124–132.
- [10] J. Ge, W. Xing, X. Xue, C. Liu, T. Lu, J. Liao, *Journal of Physical Chemistry C* 111 (2007) 17305–17310.
- [11] B. Fang, M. Kim, J.S. Yu, *Applied Catalysis B: Environmental* 84 (2008) 100–105.
- [12] S. Murugesan, K. Myers, V. Subramanian, *Applied Catalysis B: Environmental* 103 (2011) 266–274.
- [13] P. Waszczuk, T.M. Barnard, C. Rice, R.I. Masel, A. Wieckowski, *Electrochemistry Communications* 4 (2002) 599–603.
- [14] V. Mazumder, M.F. Chi, M.N. Mankin, Y. Liu, O. Metin, D.H. Sun, K.L. More, S.H. Sun, *Nano Letters* 12 (2012) 1102–1106.
- [15] D. Wang, H.L. Xin, Y. Yu, H. Wang, E. Rus, D.A. Muller, H.D. Abruna, *Journal of the American Chemical Society* 132 (2010) 17664–17666.
- [16] Y.H. Wen, R. Huang, C. Li, Z.Z. Zhu, S.G. Sun, *Journal of Materials Chemistry* 22 (2012) 7380–7386.
- [17] G. Zhang, Y. Wang, X. Wang, Y. Chen, Y. Zhou, Y. Tang, L. Lu, J. Bao, T. Lu, *Applied Catalysis B: Environmental* 102 (2011) 614–619.
- [18] Y. Pan, F. Zhang, K. Wu, Z. Lu, Y. Chen, Y. Zhou, Y. Tang, T. Lu, *International Journal of Hydrogen Energy* 37 (2012) 2993–3000.
- [19] K. Lee, S.W. Kang, S.U. Lee, K.H. Park, Y.W. Lee, S.W. Han, *ACS Applied Materials & Interfaces* 4 (2012) 4208–4214.
- [20] Y. Tang, S. Cao, Y. Chen, T. Lu, Y. Zhou, L. Lu, J. Bao, *Applied Surface Science* 256 (2010) 4196–4200.
- [21] J. Zhao, A. Sarkar, A. Manthiram, *Electrochimica Acta* 55 (2010) 1756–1765.
- [22] C. Rao, *Electrochimica Acta* 55 (2010) 3002–3007.
- [23] M. Shao, K. Sasaki, R. Adzic, *Journal of the American Chemical Society* 128 (2006) 3526–3527.
- [24] C. Koenigsmann, A.C. Santulli, K. Gong, M.B. Vukmirovic, W.p. Zhou, E. Sutter, S.S. Wong, R.R. Adzic, *Journal of the American Chemical Society* 133 (2011) 9783–9795.
- [25] Z. Peng, H. Yang, *Journal of the American Chemical Society* 131 (2009) 7542–7543.
- [26] Z. Chen, M. Waje, W. Li, Y. Yan, *Angewandte Chemie-International Edition* 46 (2007) 4060–4063.
- [27] S.M. Alia, G. Zhang, D. Kisailus, D. Li, S. Gu, K. Jensen, Y. Yan, *Advanced Functional Materials* 20 (2010) 3742–3746.
- [28] G. Zhang, L. Zhang, L. Shen, Y. Chen, Y. Zhou, Y. Tang, T. Lu, *ChemPlusChem* 77 (2012) 936–940.
- [29] F. Jia, F. Wang, Y. Lin, L. Zhang, *Chemistry - A European Journal* 17 (2011) 14603–14610.
- [30] H.W. Liang, X. Cao, F. Zhou, C.H. Cui, W.J. Zhang, S.H. Yu, *Advanced Materials* 23 (2011) 1467–1471.
- [31] X. Ge, R. Wang, P. Liu, Y. Ding, *Chemistry of Materials* 19 (2007) 5827–5829.
- [32] F.C. Meldrum, R. Seshadri, *Chemical Communications* (2000) 29–30.
- [33] Y. Song, R.M. Garcia, R.M. Dorin, H. Wang, Y. Qiu, E.N. Coker, W.A. Steen, J.E. Miller, J.A. Shelnutt, *Nano Letters* 7 (2007) 3650–3655.
- [34] M. Vondrova, T.M. McQueen, C.M. Burgess, D.M. Ho, A.B. Bocarsly, *Journal of the American Chemical Society* 130 (2008) 5563–5572.
- [35] R.S. Deshpande, S.L. Sharp-Goldman, J.L. Willson, A.B. Bocarsly, J. Gross, A.C. Finnefrock, S.M. Gruner, *Chemistry of Materials* 15 (2003) 4239–4246.
- [36] C.M. Burgess, M. Vondrova, A.B. Bocarsly, *Journal of Materials Chemistry* 18 (2008) 3694–3701.
- [37] M. Heibel, G. Kumar, C. Wyse, P. Bukovec, A.B. Bocarsly, *Chemistry of Materials* 8 (1996) 1504–1511.
- [38] B.W. Pfennig, A.B. Bocarsly, R.K. Prud'homme, *Journal of the American Chemical Society* 115 (1993) 2661–2665.
- [39] J. Xu, X. Liu, Y. Chen, Y. Zhou, T. Lu, Y. Tang, *Journal of Materials Chemistry* 22 (2012) 23659–23667.
- [40] L. Zhang, Y. Tang, J. Bao, T. Lu, C. Li, *Journal of Power Sources* 162 (2006) 177–179.
- [41] Y. Chen, Y. Zhou, Y. Tang, T. Lu, *Journal of Power Sources* 195 (2010) 4129–4134.
- [42] M. Heibel, A. Bocarsly, *Materials Science Forum* 941 (1996) 225–227.
- [43] A.X. Yin, X.Q. Min, W. Zhu, H.S. Wu, Y.W. Zhang, C.H. Yan, *Chemical Communications* 48 (2012) 543–545.
- [44] K.M. Bratlief, H. Lee, K. Komvopoulos, P. Yang, G.A. Somorjai, *Nano Letters* 7 (2007) 3097–3101.
- [45] C.X. Zhang, J.L. Zhang, B.X. Han, Y.J. Zhao, W. Li, *Green Chemistry* 10 (2008) 1094–1098.
- [46] S.I. Lim, M. Varon, I. Ojea-Jimenez, J. Arbiol, V. Puntes, *Chemistry of Materials* 22 (2010) 4495–4504.
- [47] C.T. Hsieh, J.L. Wei, J.Y. Lin, B.H. Yang, *Diamond and Related Materials* 20 (2011) 1065–1071.
- [48] H. Sun, J. Xu, G. Fu, X. Mao, L. Zhang, Y. Chen, Y. Zhou, T. Lu, Y. Tang, *Electrochimica Acta* 59 (2012) 279–283.
- [49] J. Xu, G. Fu, Y. Tang, Y. Zhou, Y. Chen, T. Lu, *Journal of Materials Chemistry* 22 (2012) 13585–13590.
- [50] M. Zheng, P. Li, G. Fu, Y. Chen, Y. Zhou, Y. Tang, T. Lu, *Applied Catalysis B: Environmental* 129 (2013) 394–402.
- [51] B. Hammer, J.K. Norskov, *Surface Science* 343 (1995) 211–220.
- [52] B. Hammer, Y. Morikawa, J.K. Norskov, *Physical Review Letters* 76 (1996) 2141–2144.
- [53] D.L. Wang, H.L. Xin, H.S. Wang, Y.C. Yu, E. Rus, D.A. Muller, F.J. DiSalvo, H.D. Abruna, *Chemistry of Materials* 24 (2012) 2274–2281.
- [54] J.K. Norskov, J. Rossmeisl, A. Logadottir, L. Lindqvist, *Journal of Physical Chemistry B* 108 (2004) 17886–17892.
- [55] L. Xiao, L. Zhuang, Y. Liu, J. Lu, H.C.D. Abruna, *Journal of the American Chemical Society* 131 (2008) 602–608.
- [56] G. Fu, W. Han, L. Yao, J. Lin, S. Wei, Y. Chen, Y. Tang, Y. Zhou, T. Lu, X. Xia, *Journal of Materials Chemistry* 22 (2012) 17604–17611.

- [57] W.P. Zhou, A. Lewera, R. Larsen, R.I. Masel, P.S. Bagus, A. Wieckowski, *Journal of Physical Chemistry B* 110 (2006) 13393–13398.
- [58] W. Zhou, J.Y. Lee, *Journal of Physical Chemistry C* 112 (2008) 3789–3793.
- [59] Y.X. Chen, M. Heinen, Z. Jusys, R.J. Behm, *Angewandte Chemie-International Edition* 45 (2006) 981–985.
- [60] Y.X. Chen, M. Heinen, Z. Jusys, R.J. Behm, *Langmuir* 22 (2006) 10399–10408.
- [61] Z. Peng, H. You, J. Wu, H. Yang, *Nano Letters* 10 (2010) 1492–1496.
- [62] U.A. Paulus, A. Wokaun, G.G. Scherer, T.J. Schmidt, V. Stamenkovic, V. Radmilovic, N.M. Markovic, P.N. Ross, *Journal of Physical Chemistry B* 106 (2002) 4181–4191.
- [63] M. Jin, H. Zhang, Z. Xie, Y. Xia, *Angewandte Chemie-International Edition* 50 (2011) 7850–7854.
- [64] B.S. Yeo, A.T. Bell, *Journal of Physical Chemistry C* 116 (2012) 8394–8400.
- [65] Y. Chen, G. Zhang, J. Ma, Y. Zhou, Y. Tang, T. Lu, *International Journal of Hydrogen Energy* 35 (2010) 10109–10117.
- [66] D.H. Lim, D.H. Choi, W.D. Lee, H.I. Lee, *Applied Catalysis B: Environmental* 89 (2009) 484–493.